# Phase behavior and dynamics of active Brownian particles in an alignment field

Sameh Othman [1,*] Jiarul Midya [1,2,†] Thorsten Auth [1,‡] and Gerhard Gompper [1,§]

[1]*Theoretical Physics of Living Matter, Institute of Biological Information Processing and Institute for Advanced Simulation, Forschungszentrum Jülich, 52425 Jülich, Germany*

[2]*School of Basic Sciences, Indian Institute of Technology, Bhubaneswar 752050, India*

(Received 13 February 2024; revised 5 November 2024; accepted 20 December 2024; published 21 January 2025)

Self-propelled particles that are subject to noise are a well-established generic model system for active matter. A homogeneous alignment field can be used to orient the direction of the self-propulsion velocity and to model systems like phoretic Janus particles with a magnetic dipole moment or magnetotactic bacteria in an external magnetic field. Computer simulations are used to predict the phase behavior and dynamics of self-propelled Brownian particles in a homogeneous alignment field in two dimensions. Phase boundaries of the gas-liquid coexistence region are calculated for various Péclet numbers, particle densities, and alignment field strengths. Critical points and exponents are calculated and, in agreement with previous simulations, do not seem to belong to the universality class of the 2D Ising model. Finally, the dynamics of spinodal decomposition for quenching the system from the one-phase to the two-phase coexistence region by increasing the Péclet number is characterized. Our results may help to identify parameters for optimal transport of active matter in complex environments.

DOI: 10.1103/PhysRevE.111.015425

## I. INTRODUCTION

Active matter is abundant in life and ranges from the cytoskeleton [1], tissues [2], and biofilms [3] on the microscale to fish schools [4], animal herds [5], and pedestrian crowds [6] on the macroscale. In synthetic and engineered systems, phoretic Janus particles are a versatile model system on the microscale [7–10], and small robots and vibrated granular matter on the macroscale [11,12]. The systems consist of individual self-propelled agents, and thus are intrinsically out-of-equilibrium and show complex emergent collective behavior [13,14]. However, there is no general concept for predicting the phase behavior analogous to the minimization of the free energy at thermal equilibrium. Only in very few cases, such as for spherical and rodlike self-propelled particles and filament-motor mixtures, analytical expressions have been proposed to predict phase behavior [15,16]; phase-separation kinetics has been studied by numerical analysis of continuum theory [17]. Therefore, high-performance computing is often the method of choice to characterize the structure and dynamics of nonequilibrium systems.

A well-established generic model system for dry active matter is active Brownian particles (ABPs), whose motion, in addition to their self-propulsion velocity, is subject to thermal noise. Intriguingly, ABPs exhibit motility-induced phase separation (MIPS) at high densities, blocking each other's motion and leading to cluster formation. Analogous to the vapor-liquid transition in passive systems, high-density liquid clusters of ABPs coexist with a low-density active gas phase, however, without any attraction. Cooperative motion has been detected in three-dimensional dense suspensions of ABPs despite the lack of an alignment mechanism. It has been hypothesized that this collective swirling motion is driven by an interface-sorting process [18].

Critical points characterized by power laws with universal exponents are a prevalent aspect of second-order phase transitions, such as the critical point of the gas-liquid coexistence. Previous simulation studies of two-dimensional (2D) ABP systems have accurately mapped out the binodals and estimated the location of the critical point [19]. It has been shown that the associated critical exponents are different from the standard 2D Ising universality class. In contrast, the dynamical critical exponent, related to the relaxation dynamics of the system after a quench from a homogeneous state below the critical point to the two-phase region, is consistent with the 2D Ising universality class [20]. The controversy regarding the universality class remains alive and demands further investigation.

An interesting system is ABPs in an alignment field for the direction of their self-propulsion, see Fig. 1. It can be experimentally realized by magnetic particles with a dipole moment that can couple to an external magnetic field, which is routinely used for magnetic microrheology [21] and which can be employed to generate anisotropic elastic materials [22]. For low densities and sufficiently weak magnetic dipole moments, the mutual interaction between magnetic colloids can be neglected, whereas, for higher densities and strong dipole moments, a magnetic alignment of the dipoles has to be taken into account [23]. For varying self-propulsion velocities and magnetic field strengths in the presence of hydrodynamic interactions, traveling sheets and dynamic aggregates of magnetic microswimmers have been numerically predicted [24,25]. However, an alignment of the direction of the propulsion velocity is not limited to magnetic-dipole interactions. Also interactions inspired by the ferromagnetic

*Contact address: s.othman@fz-juelich.de
†Contact address: jmidya@iitbbs.ac.in
‡Contact address: t.auth@fz-juelich.de
§Contact address: g.gompper@fz-juelich.de

 

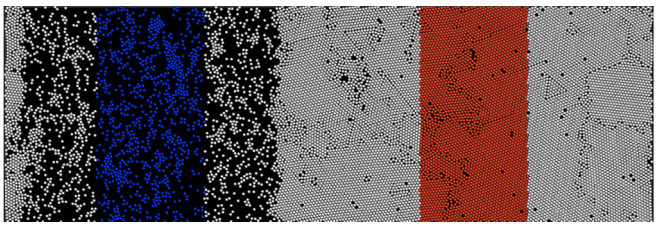

FIG. 1. Simulation snapshot of a system that contains 12 576 particles in a box with dimensions of $L_x = 80\sigma$, $L_y = 240\sigma$ at Pe = 144 with an alignment field of strength $\tilde{B} = 2$ in the $y$ direction. Two stacked square boxes with side lengths $\ell_s = 40\sigma$, placed at the centers-of-mass of the liquid (red) and the gas phase (blue), are used to measure the particle densities.

four-state Potts model [26], excluded-volume interactions of particles with elongated shapes [27,28], and visual perception [29,30] may lead to a velocity alignment. The most prominent example for a theoretical description of aligning systems is the Vicsek model, where alignment interactions between self-propelled agents orient their direction of motion with respect to the orientations of their neighbors [31].

In this work, we use Brownian dynamics simulations to study the critical behavior of two-dimensional ABP systems subject to a homogeneous external alignment field that couples to the direction of the ABP self-propulsion velocities. Phase-separated systems show characteristic stripe patterns that are oriented parallel to the direction of the field. In addition to steady states, we simulate and analyze the domain coarsening dynamics after quenches from the one-phase to the two-phase region. Here, we distinguish between the directions parallel and perpendicular to the field. For the striped structures, we find a much faster growth of cluster size in the direction parallel to the alignment field compared with the direction perpendicular to the field.

The remainder of the manuscript is organized as follows. In Sec. II, we introduce the system and the simulation technique. In Sec. III, we predict the two-phase gas-liquid coexistence region, the critical points, and the critical exponents for various alignment field strengths. In Sec. IV, we discuss spinodal decomposition for a quench from points in the phase space with Péclet numbers below the critical point into the two-phase coexistence region. Finally, in Sec. V, we summarize our results and provide an outlook.

## II. MODEL AND METHODS

We use Brownian dynamics simulations to simulate the motion of ABPs in two dimensions in an external alignment field $\tilde{\mathbf{B}}$, which is governed by the equations of motion

$$\dot{\mathbf{r}} = \gamma_{\mathrm{T}}^{-1}\mathbf{F} + v_0\hat{\mathbf{e}} + \sqrt{2\mathrm{D_T}}\boldsymbol{\xi}_{\mathrm{T}} \tag{1}$$

$$\dot{\hat{\mathbf{e}}} = \gamma_{\mathrm{R}}^{-1}\mu\hat{\mathbf{e}} \times (\tilde{\mathbf{B}} \times \hat{\mathbf{e}}) + \sqrt{2\mathrm{D_R}}\boldsymbol{\xi}_{\mathrm{R}} \times \hat{\mathbf{e}}, \tag{2}$$

where $\mathbf{r}$ is the position and $\hat{\mathbf{e}} = (\sin\theta, \cos\theta)^T$ the orientation of the particle. Here, $\gamma_{\mathrm{T}}$ and $\gamma_{\mathrm{R}}$ are the translational and rotational friction coefficients, respectively. These are the Gaussian-distributed random noises with unit variance: $\boldsymbol{\xi}_{\mathrm{T}}$ is a vector in the plane of the particle's motion and $\boldsymbol{\xi}_{\mathrm{R}}$ is a vector perpendicular to this plane. The translational diffusion coefficient is $D_{\mathrm{T}} = k_B\mathrm{T}/\gamma_{\mathrm{T}}$ with the Boltzmann constant $k_B$ and the temperature T. The relation between the rotational and translational diffusion coefficients is $D_{\mathrm{R}} = 3D_{\mathrm{T}}/d_{\mathrm{BH}}^2$, which applies to spherical colloids in a Newtonian fluid in 3D [32]. Each particle possesses a self-propulsion velocity $v_0\hat{\mathbf{e}}_i$, which is constant in magnitude and parallel to the dipole moment $\boldsymbol{\mu} = \mu\hat{\mathbf{e}}_i$ of the particle that couples to an external alignment field $\mathbf{B}$. The angular velocity of the particle is

$$\dot{\theta} = \sqrt{2\mathrm{D_R}}\xi_{\mathrm{R}} + \gamma_{\mathrm{R}}^{-1}\mu|\tilde{\mathbf{B}}|\sin\theta, \tag{3}$$

with the orientation angle $\theta$ of the particle dipole moment with respect to the direction of the alignment field.

The particle-particle interaction is taken into account by the force $\mathbf{F}$, which is derived from the purely repulsive Weeks-Chandler-Andersen (WCA) potential

$$\mathrm{U_{WCA}(r)} = \begin{cases} 4\epsilon\left[\left(\frac{\sigma}{r}\right)^{12} - \left(\frac{\sigma}{r}\right)^{6} + 1/4\right] & r < 2^{1/6}\sigma \\ 0 & r \geqslant 2^{1/6}\sigma \end{cases}, \tag{4}$$

where $r$ is the distance between two particles, and $\epsilon$ characterizes the height and $\sigma$ the width of the potential. The potential vanishes at $r_{\mathrm{min}} = 2^{1/6}\sigma$, where we truncate the potential. The effective particle radius at thermal equilibrium is defined as the Barker-Henderson diameter $d_{\mathrm{BH}}/\sigma = \int_0^{r_{\mathrm{min}}} dr\,[1 - \exp(-U_{WCA}(r)/k_BT)]$. By setting $\epsilon = 100\,k_B\mathrm{T}$, we ensure the particles behave similar to hard spheres with diameter $d_{\mathrm{BH}}/\sigma = 1.10688$. In the following, we use the characteristic timescale $\tau_R = 1/D_{\mathrm{R}}$ for the rotation of the particle dipole moments as a time unit. We use the Péclet number $\mathrm{Pe} = 3v_0/(d_{\mathrm{BH}}D_{\mathrm{R}}) = v_0 d_{\mathrm{BH}}/D_{\mathrm{T}}$ to characterize the self-propulsion.

Our technique for the calculation of order parameters and phase diagrams is based on Ref. [33]. We initialize the systems by placing $N$ particles randomly in rectangular or square simulation boxes with periodic boundary conditions at various particle packing fractions $\phi = \pi d_{BH}^2\rho/4$, where $\rho$ is the number density of the particles. The rectangular simulation boxes assist phase separation into slabs with high and low densities, within which two stacked square boxes are used to measure the particle packing fractions, see Fig. 1. Our algorithm independently detects the widest slabs of the liquid and the gas phase to place the boxes. For the phase-diagram calculations, each point on the figure is the average over at least five randomly initialized simulations with simulation time $tD_{\mathrm{R}} = 1952$ each. The critical point is determined using Binder cumulants; each value of the cumulant is the average over at least 30 simulations, see also the discussion in the Supplemental Material (SM) [34]. We use LAMMPS to perform the simulations, see Appendix for the values of the simulation parameters and further details of the simulations.

## III. PHASE DIAGRAMS AND CRITICAL BEHAVIOR

Above a critical Péclet number $\mathrm{Pe_{cr}}$ and for intermediate packing fractions $\phi$, we observe the coexistence of a high-density liquid phase and a low-density gas phase. We calculate the packing fractions of both phases from one simulation at values of Pe in the two-phase region and approximately the critical packing fraction $\phi \approx \phi_{\mathrm{cr}}$, see Figs. 1 and 2(a). Without an alignment field ($\tilde{B} = 0$), the coexisting packing fractions of the gas and the liquid phase agree well with those reported

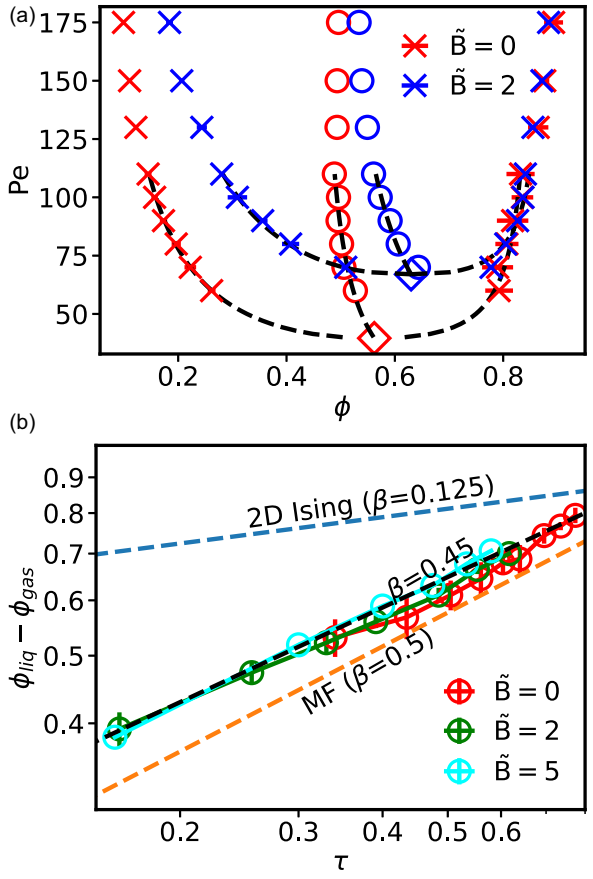


FIG. 2. Critical points of ABP systems. (a) Boundaries for the gas-liquid coexistence region for the alignment field strengths $\tilde{B} = 2$ (blue) and $\tilde{B} = 0$ (red). Crosses mark the phase boundaries, diamonds the critical points, and circles the values of the rectilinear diameter $\phi_d$, compare Eq. (6). (b) Order parameter $\phi_{liq} - \phi_{gas}$ vs the distance to the critical point $\tau$ for alignment fields $\tilde{B} = 0$, 2, and 5 and measured power-law exponents $\beta$. The exponents for 2D Ising and mean-field (MF) systems are shown for comparison.

previously [33], see Fig. S3(b). The difference between the liquid and gas packing fractions increases with increasing dimensionless "distance" $\tau = (\mathrm{Pe}_{cr}^{-1} - \mathrm{Pe}^{-1})/\mathrm{Pe}_{cr}^{-1}$ from the critical point,

$$\phi_{liq} - \phi_{gas} = c_1 \tau^{\beta} \tag{5}$$

with the critical exponent $\beta$. The rectilinear diameter

$$\phi_d = \frac{\phi_{liq} + \phi_{gas}}{2} = \phi_{cr} + c_2 \tau + O(\tau^2) \tag{6}$$

is the arithmetic mean of $\phi_{gas}$ and $\phi_{liq}$; the line depicting the rectilinear diameters ends at the critical point at $\phi_{cr}$ and $\mathrm{Pe}_{cr}$. In the presence of an alignment field, the area of the two-phase regions shrinks compared to the system without field, see Fig. 2(a). Whereas at high values of Pe the boundary of the two-phase region at high packing fractions is almost unchanged compared with $\tilde{B} = 0$, the boundary at low packing fractions significantly shifts to higher $\phi$. Therefore, for fixed Pe, the rectilinear diameter $\phi_{d,\tilde{B}=2}$ increases with increasing field strength.

With the help of the power-law dependence of $\phi_{liq} - \phi_{gas}$ on $\tau$ in the range $0.15 < \tau < 0.7$, see Eq. (5), we find a critical exponent $\beta \approx 0.45$ for $\tilde{B} = 0$, 2, and 5, see Fig. 2(b). Thus, the critical exponent in the presence of a finite alignment field is similar to the critical exponent without. Therefore, we hypothesize that the critical behavior found for the gas-liquid coexistence of ABPs with and without alignment field belongs to the same universality class. As reported earlier for ABPs without alignment field [33], the critical exponent is much higher than $\beta_{2D\,\mathrm{Ising}} = 0.125$ for a 2D Ising system and slightly lower than $\beta_{MF} = 0.5$ for a mean-field model [35].

To determine the locations of the critical points more precisely, we calculate the cumulants [33]

$$Q_{\ell_s} = \frac{\langle m^2 \rangle_{\ell_s}^2}{\langle m^4 \rangle_{\ell_s}} \tag{7}$$

following the procedure described in Ref. [36], see Figs. S3(b), S4, and S5. Here, the second and the fourth moments of the order parameter are defined as

$$\langle m^n \rangle_{\ell_s} = \frac{1}{4}\left[\sum_{i=1}^{2}((\phi_{\mathrm{gas},\ell_s,\mathrm{i}} - \phi_d)^n + (\phi_{\mathrm{liq},\ell_s,\mathrm{i}} - \phi_d)^n)\right] \tag{8}$$

with $n = 2$ and 4, respectively. The packing fractions $\phi_{\mathrm{gas},\ell_s,\mathrm{i}}$ and $\phi_{\mathrm{liq},\ell_s,\mathrm{i}}$ are measured in sub-boxes of size $\ell_s \times \ell_s$ in the gas and the liquid phase, respectively; the index $i$ distinguishes the two stacked square boxes indicated in Fig. 1. We study system sizes up to $\ell_s = 20$ for the calculation of cumulants. For larger sizes, $\ell_s = 50$, 100, and 150, we are unable to obtain the formation of single gas and liquid slabs. This is probably due to the very low line tension in ABP systems, for which even the sign is still under debate and depends on the calculation technique [16,37]. It prevents us from placing boxes surrounded by the same phase as suggested in Refs. [33,36]. In the Supplemental Material (SM) [34], we show that the slope of the cumulants $Q_{\ell_s}$ with $\tau$ at the critical point increases as a power law with the sub-box size $\ell_s$,

$$dQ_{\ell_s}/d\tau|_{\tau \simeq 0} \propto \ell_s^{1/\nu} \tag{9}$$

with $\nu \approx 1.5$, which is consistent with the value for the 2D Ising model. We find the same critical exponents for $\tilde{B} = 2$ and $\tilde{B} = 0$.

With increasing alignment field strength, the critical points shift to higher packing fractions $\phi_{cr}$ and Péclet numbers $\mathrm{Pe}_{cr}$. We fit the dependence of the coordinates of the critical points on the field strength as

$$\phi_{cr} = 0.56 + 0.07\,\tilde{B}^{1/3} - 0.016\,\tilde{B}^{1/2} \tag{10}$$

$$\mathrm{Pe}_{cr} = 32.23 + 19.09\,\tilde{B} + 3.42\,\tilde{B}^2 \tag{11}$$

and collapse the phase boundaries for the two-phase coexistence region for various alignment field strengths, see Fig. 3. The good agreement of the normalized data supports the conclusion that the systems for all alignment field strengths belong to the same universality class.

## IV. DOMAIN COARSENING DYNAMICS

Next, we investigate the effect of an alignment field on the kinetics of domain growth following quenches from outside

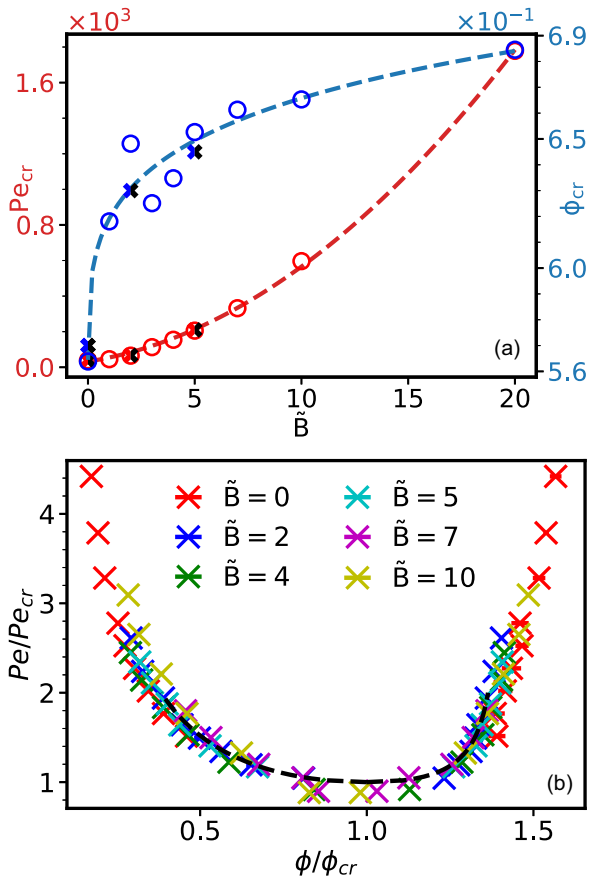


FIG. 3. Critical point positions and boundaries of the two-phase coexistence region for various alignment field strengths. (a) Coordinates of the critical points as function of the alignment field strength $\tilde{B}$, determined using cumulants (crosses) or by assuming $\beta = 0.45$ and simultaneously fitting the data using Eqs. (5) and (6); the fit functions (dashed lines) are given by Eqs. (10) and (11). (b) Normalized coexisting phase diagrams for various values of $\tilde{B}$ and fit for $\tilde{B} = 0$.

($\phi = \phi_{\rm cr}$, Pe $= 10$) to deep inside ($\phi = \phi_{\rm cr}$, Pe $\simeq 3\,$Pe$_{\rm cr}$) the coexistence region, see Fig. S7 in the SM [34]. Figure 4 shows the spinodal decomposition for $\tilde{B} = 0$, Fig. 5 for $\tilde{B} = 2$; videos can be found in the Supplemental Material. We characterize the dynamics using the equal time two-point order-parameter correlation function [38]

$$C(\mathbf{r}, t) = \langle \psi(\mathbf{0}, t)\psi(\mathbf{r}, t)\rangle - \langle \psi(\mathbf{0}, t)\rangle\langle \psi(\mathbf{r}, t)\rangle, \quad (12)$$

where $\psi(\mathbf{r}, t)$ is the space- and time-dependent order parameter introduced in Sec. S4 A of the SM [34]. At early times, $tD_{\rm R} \lesssim 1$, the domain patterns both for $\tilde{B} = 2$ and $\tilde{B} = 0$ are isotropic in space and $C(x, y = 0, t) \approx C(x = 0, y, t)$, compare Figs. 4, 5, and 6. At later times, $tD_{\rm R} > 1$, for $\tilde{B} = 2$ first elongated clusters and eventually stripe patterns form in the direction of the alignment field; the correlation functions $C(x, y = 0, t)$ transverse and $C(x = 0, y, t)$ parallel to the direction of the alignment field differ. Interestingly, the average velocity of the particles in the direction of the alignment field in the gas phase is higher than in the liquid phase, i.e., $\langle v_{\rm y,gas}\rangle - \langle v_{\rm y,liq}\rangle > 0$, see Fig. S15 in the SM [34]. As a result, particles from the gas phase get deposited on the back of nucleated clusters. The deviation of the simulation data in

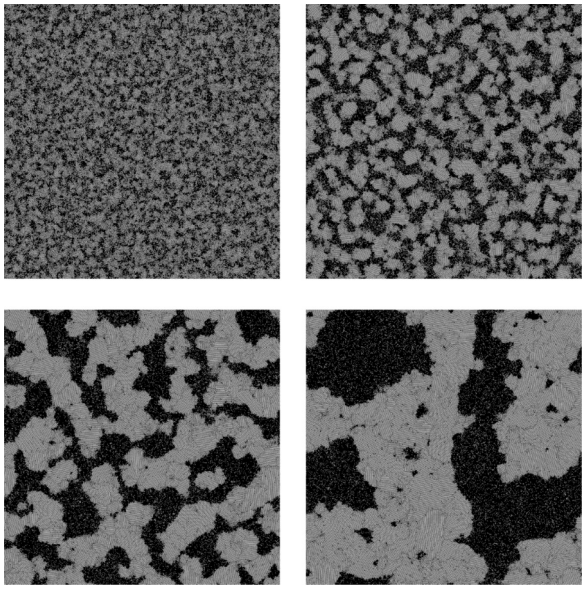

FIG. 4. Snapshots of a 2D ABP system with packing fraction $\phi = 0.60$, alignment field strength $\tilde{B} = 0$, and system size $512\sigma \times 512\sigma$ at various times after quenching from Pe $= 10$ to Pe $= 132$: $tD_{\rm R} = 0.39$ (top left), $tD_{\rm R} = 1.85$ (top right), $tD_{\rm R} = 14.84$ (bottom left), and $tD_{\rm R} = 337.36$ (bottom right). See also Video 1 in the SM [34].

Fig. 7 at late times from the power law is associated with the finite-size effects appearing much earlier in $\ell_y$ than in $\ell_x$.

We characterize the sizes $\ell_y$ and $\ell_x$ of the domains parallel and perpendicular to the alignment field from the decays of $C(x = 0, y, t)$ and $C(x, y = 0, t)$ to 1/4 of their initial values, respectively. Whereas the domains perpendicular to the

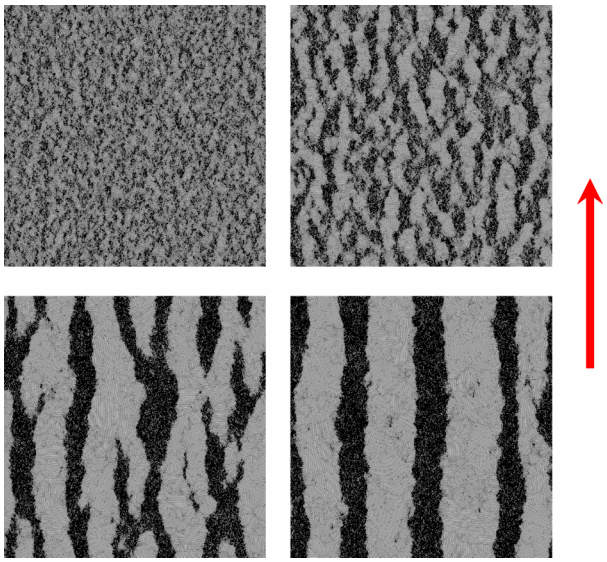

FIG. 5. Snapshots of a 2D ABP system with packing fraction $\phi = 0.63$, alignment field strength $\tilde{B} = 2$ (red arrow), and system size $512\sigma \times 512\sigma$ at various times after quenching from Pe $= 10$ to Pe $= 221$: $tD_{\rm R} = 0.39$ (top left), $tD_{\rm R} = 1.85$ (top right), $tD_{\rm R} = 14.84$ (bottom left), and $tD_{\rm R} = 337.36$ (bottom right). See also Videos 2 and 3 in the SM [34].

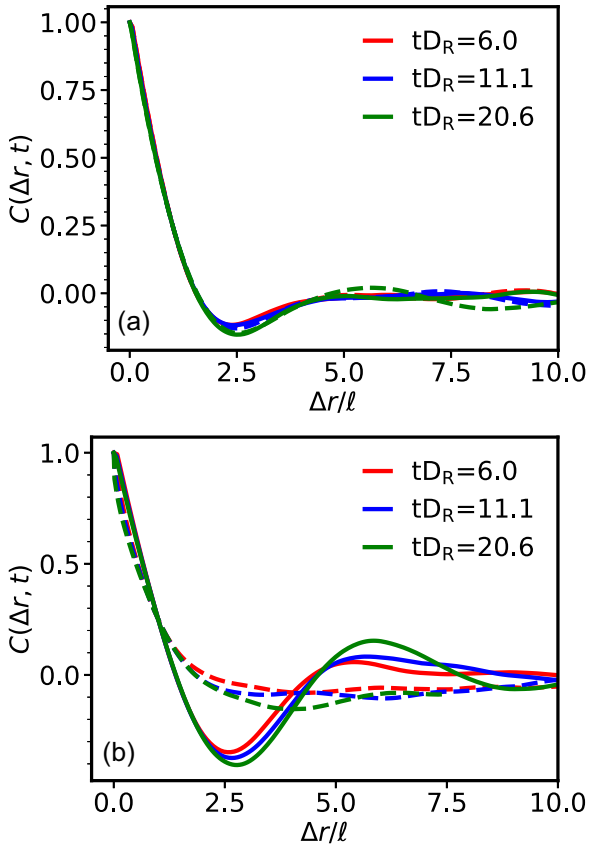


FIG. 6. Two-point order-parameter correlation functions $C(\Delta\mathbf{r}, t)$ at different times, scaled by the average domain length $\ell$, for (a) $\tilde{B} = 0$ and (b) $\tilde{B} = 2$. The solid line indicates the correlation function along the $x$ axis, and the dashed line along the $y$ axis.

alignment field grow as $\ell_x \propto t^{\alpha}$ with $\alpha = 1/3$, similar to the field-free system, we find a much faster domain growth, $\ell_y \propto t^{2/3}$, parallel to the field, see Fig. 7. The domain growth perpendicular to the field direction is dominated by the particle evaporation-condensation Lifshitz-Slyozov mechanism

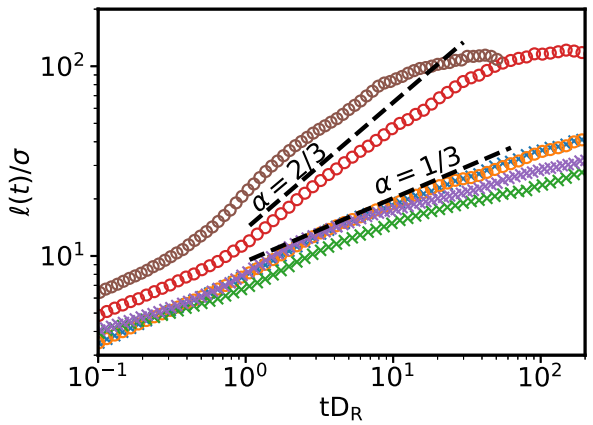


FIG. 7. Domain length as a function of time for the quenched system, calculated from the two-point correlation functions decaying to $C(\Delta r, t) = 0.25$ in Fig. 6, for $\tilde{B} = 0$ (blue, orange), $\tilde{B} = 2$ (green, red), and $\tilde{B} = 5$ (purple, brown). Circle symbols indicate the $y$ component, crosses the $x$ component.

for Ostwald ripening, leading to $\ell_x \propto t^{1/3}$ [39–41], which has been previously observed for the phase separation of active Brownian particles for $\tilde{B} = 0$ [20].

The faster growth, $\ell_y \propto t^{2/3}$, suggests domain growth via merging of clusters. After subtracting the average velocity from the alignment field, we observe slow movement of the clusters opposite to the direction of the field. The average particle velocity in the gas phase is higher than in the cluster phase, causing clusters to "collect" particles at their rear; the clusters get elongated in the field direction, see Figs. S14 and S15 in the SM [34]. These result in merging of clusters along the field direction and the higher growth exponent. A similar growth exponent of $\alpha = 2/3$ is observed in phase-separating passive systems in the inertial hydrodynamic regime [38]. Accelerated cluster growth with exponents $\alpha \approx 0.7$ has also been reported for phase-separating active systems with Vicsek-like alignment [42–44], and for systems of active Brownian disks without alignment field [45].

Because the domain lengths show power-law growth $\ell \sim t^{\alpha}$, we expect the patterns to be statistically self-similar. Indeed, by dividing the correlation functions $C(x, y = 0, t)$ and $C(x = 0, y, t)$ by the corresponding average domain lengths $\ell_x(t)$ and $\ell_y(t)$, respectively, the correlation functions for fixed alignment field strength and direction collapse on master curves, see Fig. 6. For $\tilde{B} = 0$, the correlation functions decay, assume negative values for $2 \lesssim \Delta r/\ell \lesssim 4$, and remain approximately zero for $\Delta r/\ell \gtrsim 4$, see Fig. 6(a). For $\tilde{B} = 2$, we find strong and long-reaching oscillations in $C(x, y = 0, t)$, reflecting the stripe pattern being oriented along the $y$ direction parallel to the field, see Fig. 6(b). The correlation in the direction of the field $C(x = 0, y, t)$ decays without any overshoot to zero already for $\Delta r/\ell \gtrsim 3$.

The relaxation of the nonequilibrium ABP systems approaching steady states via domain coarsening can also be characterized using the two-time order-parameter correlation function [46]

$$C_{\mathrm{ag}}(t, t_w) = \langle \psi(\mathbf{r}, t)\psi(\mathbf{r}, t_w)\rangle - \langle \psi(\mathbf{r}, t)\rangle\langle \psi(\mathbf{r}, t_w)\rangle. \quad (13)$$

Here, $t$ and $t_w$ (with $t > t_w$) are the observation time and the waiting time after the quench, respectively. For passive systems in equilibrium, $C_{\mathrm{ag}}(t, t_w)$ exhibits time-translational invariant properties, i.e., the data for $C_{\mathrm{ag}}(t, t_w)$ vs $(t - t_w)$ collapses for different choices of $t_w$. For out-of-equilibrium systems, the decay of $C_{\mathrm{ag}}(t, t_w)$ becomes slower with increasing waiting time $t_w$, thus, violates the above invariance. For the phase-separation kinetics of passive systems, Refs. [47] and [46] predicted a power-law scaling of $C_{\mathrm{ag}}(t, t_w)$ as a function of $t/t_w$ as

$$C_{\mathrm{ag}}(t, t_w) \sim \left(\frac{t}{t_w}\right)^{-\lambda_{\mathrm{ag}}}, \quad (14)$$

where the aging exponent $\lambda_{\mathrm{ag}}$ determines the relaxation rate of the nonequilibrium systems.

For $\tilde{B} = 0$, $C_{\mathrm{ag}}(t, t_w)$ as a function of $t/t_w$ for different waiting times $t_w$ collapses onto a single master curve with $\lambda_{\mathrm{ag}} = 1$, see Fig. S12 in the SM [34]. The predicted value of $\lambda_{\mathrm{ag}}$ is consistent with the value reported in Ref. [46]. The value of the aging exponent $\lambda_{\mathrm{ag}}$ is sensitive to various features, such as the conservation of order parameters and space dimen-

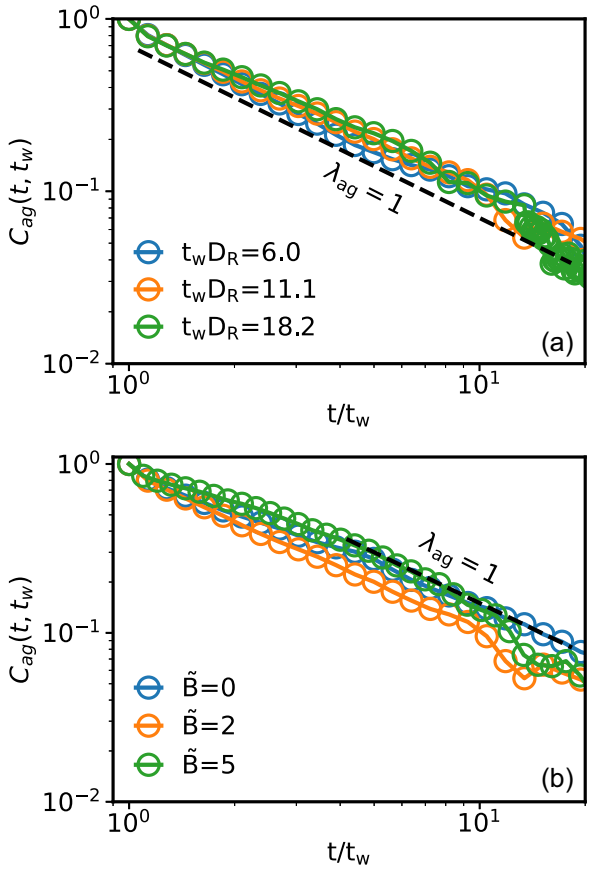


FIG. 8. Two-time order-parameter correlation function $C_{\rm ag}(t, t_{\rm w})$ versus $t/t_w$ (a) for alignment-field strength $\tilde{B} = 2$ and various waiting times, and (b) for waiting time $t_{\rm w}D_{\rm R} = 11.1$ and various alignment-field strengths.

sionality. For passive systems with conserved order-parameter dynamics, $\lambda_{\rm ag}$ satisfies the lower bound $\lambda_{\rm ag} \geqslant \alpha(\beta_s + d)/2$, where $d$ is the space dimensionality, and $\beta_s$ is associated with the small-$k$ power-law behavior of the structure factor $S(\mathbf{k}, t)$, the Fourier transformation of $C(\mathbf{r}, t)$ [48]. For phase-separating $2D$ ABP systems with $\tilde{B} = 0$, the small-$k$ power-law behavior of $S(\mathbf{k}, t)$ is consistent with $\beta_s \simeq 3$ [20], which sets the lower bound $\lambda_{\rm ag} > 2.5\alpha \approx 0.8$ for $\alpha = 1/3$.

For $\tilde{B} = 0$, the scaling of $C_{\rm ag}(t, t_w)$ as a function of $t/t_w$ is presented in Fig. S12 in the SM [34]. The master curve for the data from different values of $t_w$ follows a power-law decay with an exponent $\lambda_{\rm ag} = 1$. The predicted value of $\lambda_{\rm ag}$ is consistent with the value reported in Ref. [46].

For $\tilde{B} = 2$, $C_{\rm ag}(t, t_w)$ as a function of $t/t_w$ shows strong periodic oscillations with decaying amplitudes for increasing times, see Fig. S11 in the SM [34]. The oscillations are associated with flow in the system along the field direction and the presence of periodic boundary conditions; see the SM [34] for more details. Therefore, we analyze the correlations after subtracting the average velocity of the particles along the field direction, see Fig. 8(a). The resulting master curve then decays with the same exponent $\lambda_{\rm ag} = 1$ as in the case of $\tilde{B} = 0$. We observe scaling of $C_{\rm ag}(t, t_w)$ for different alignment fields, and the master curve shows a power-law decay with the same exponent $\lambda_{\rm ag} = 1$, see Fig. 8(b). This indicates that the relaxation dynamics of the 2D ABP systems does not depend on the strength of the alignment field. As an alternative approach to subtracting the average particle velocity, we have analyzed the temporal correlation function $C_{\rm dyn}(t, t_{\rm w})$ of the particle densities in the vicinity of selected particles, which we discuss in the SM [34]. Interestingly, the master curves exhibit a power-law decay $C_{\rm dyn}(t, t_{\rm w}) \sim (t/t_w)^{-\lambda_{\rm ag}^{\rm dyn}}$ with $\lambda_{\rm ag}^{\rm dyn} = 2$ for $\rm B = 2$ and $\rm B = 0$, which again indicates that the presence of an alignment field for the direction of the propulsion velocity does not affect the relaxation dynamics of 2D ABP systems.

## V. SUMMARY AND CONCLUSIONS

We have studied phase behavior and dynamics of domain growth in two-dimensional systems of APBs subject to a homogeneous external alignment field by systematically varying the strength of the alignment field. The systems have been simulated using overdamped dynamics in rectangular simulation boxes, with stacked square boxes within slabs of liquid and gas phases to determine the particle packing fractions. The system size is limited by the size above which phase separation occurs in several smaller domains, which also limits the accuracy of determining the critical-point coordinates. The critical Péclet numbers and packing fractions for gas-liquid coexistence increase with increasing field strength. The different binodals fall on a single master curve when the Péclet number is normalized with the critical Péclet number $\rm Pe_{cr}$ and the packing fraction with the critical packing fraction $\phi_{\rm cr}$, which indicates that the order-parameter critical exponent $\beta$ is independent of the presence of an external field. Furthermore, we estimate $\beta \approx 0.45$, which lies inbetween the values for the mean-field and 2D Ising universality classes. Our prediction is consistent with the previously reported value for 2D ABP systems without alignment field ($\tilde{B} = 0$) [33].

We have also studied the dynamics of domain growth following quenches of the systems from outside to deep inside the coexistence region. The isotropicity and self-similarity of the evolution of percolating domain patterns are characterized via the 1D two-point order-parameter correlation functions $C(x, y = 0, t)$ and $C(x = 0, y, t)$. For $\tilde{B} = 0$, in agreement with Ref. [20], we show that the domain growth occurs as $\ell_x \sim \ell_y \sim \ell \sim t^{1/3}$, following the Lifshitz-Slyozov mechanism. For $\tilde{B} = 2$, the formation of anisotropic domain growth is observed, with stripe patterns eventually developing parallel to the field direction. This leads to different power laws for the domain growth parallel and perpendicular to the field. The domain growth of the domain size along the field direction follows the power-law $\ell_y \sim t^{2/3}$, whereas transverse to the field direction the growth follows the same power law as for $\tilde{B} = 0$, $\ell_x \sim t^{1/3}$. The decay of the autocorrelation function of the phase at a fixed point in space, $C_{\rm ag}(t, t_w) \sim (t/t_w)^{-\lambda_{\rm ag}}$ with exponent $\lambda_{\rm ag} = 1$, characterizes the relaxation dynamics of the system. The decay exponent $\lambda_{\rm ag}$ does not depend on the alignment field strength, indicating that the relaxation dynamics of 2D ABP systems does not change in the presence of the external field.

In conclusion, ABPs that are subject to a homogeneous external alignment field that couples to a dipole moment parallel to the direction of their self-propulsion velocity move on average along the field direction. However, in a comoving ref-

erence frame, such systems can be characterized analogously to ABPs without an alignment field. Furthermore, the presence of the alignment field does not change the universality class of gas-liquid phase separation in 2D systems of ABPs, such that the critical points are characterized by the same critical exponents for different alignment field strengths and the coordinates of the critical points can be determined without the need for a cumulant analysis. However, the effective self-propulsion velocity and thus Péclet number of the particles in the comoving reference frame are reduced compared to alignment-field-free systems that have identical thermal noise and self-propulsion velocities in the laboratory reference frame. Therefore, an overall alignment of the direction motion does not only generate an overall particle flux, but also shifts the two-phase coexistence region to higher Péclet numbers and particle packing fractions.

Directed motion and transport of active particles are ubiquitous in living and synthetic systems. The motion of animal herds to new food sources and of magnetotactic bacteria in an external magnetic field are well-known examples. For synthetic particles, alignment induced by external fields is the simplest way to manipulate the overall motion of the particles in a system. In contrast to other techniques to generate an overall particle flux, such as structured channel boundaries [49], external fields also have the advantage that their strength and direction can be readily controlled and varied.

## ACKNOWLEDGMENTS

J.M. thanks P. Virnau (Mainz) and S. Majumder (Amity University Noida, India) for discussions on critical behavior of active Brownian particles. T.A. thanks Kyongok Kang and Jan K. G. Dhont (Jülich) for discussions on phase separation. This work was supported by the Federal Ministry of Education and Research of Germany in the framework of the Palestinian-German Science Bridge (BMBF Grant No. 01DH16027). All authors acknowledge a computing time grant on the supercomputer JURECA at the Jülich Supercomputing Centre. We thank the Exploratory Research Space of RWTH Aachen University for fostering stimulating conceptual discussions within the project "Synthesizing Life-Like Material Systems."

## APPENDIX: SIMULATION PARAMETERS

All simulations are performed through molecular dynamics (MD) simulations using LAMMPS [50]. We simulate ABPs in rectangular simulation boxes with aspect ratio 1 : 3 with various system sizes up to $80\sigma \times 240\sigma$ for cumulant analysis, and in square boxes of size $1024\sigma \times 1024\sigma$ for domain-coarsening dynamics. The particles are defined using the hybrid atom style "dipole sphere" of LAMMPS, which adds a dipole moment to the particles whose orientation changes due to rotational diffusion and couples to an alignment field. The particle positions and dipole orientations are updated using the fix "brownian/sphere", which implements a velocity Verlet algorithm for overdamped particle dynamics. Throughout the simulation, we set $T^* = Tk_B/\epsilon = 1$, $\gamma_T = \epsilon\sigma^2$, $\gamma_r = 0.40839\epsilon\sigma^2$, and use independent Gaussian-distributed noises $\boldsymbol{\xi}_T$ and $\boldsymbol{\xi}_R$ with unit variance.

Initially, the particles are randomly distributed using a new random seed for every run and restart of a simulation. For new simulations, the "minimize" function is used to ensure that the particles are not overlapping. We start with a run of $10^6$ time steps to obtain a steady state. The integration time step is $\Delta t = 2.44\times10^{-6}D_R^{-1}$ for all systems. The force distributions for particle-particle interactions for $\tilde{B} = 0, 2$, and 10 in Fig. S16 of the SM [34] demonstrate that, despite the huge difference of typical Péclet numbers for the various field strengths, typical interparticle forces are similar. For a full production run, we then simulate for $8\times10^8$ time steps. All analysis of LAMMPS dump files have used OVITO [51] and Python.

[1] V. Schaller, C. Weber, C. Semmrich, E. Frey, and A. R. Bausch, Nature (London) **467**, 73 (2010).
[2] W. Xi, T. B. Saw, D. Delacour, C. T. Lim, and B. Ladoux, Nat. Rev. Mater. **4**, 23 (2019).
[3] H. Jeckel, F. Díaz-Pascual, D. J. Skinner, B. Song, E. Jiménez-Siebert, K. Strenger, E. Jelli, S. Vaidya, J. Dunkel, and K. Drescher, PLoS Biol. **20**, e3001846 (2022).
[4] J. K. Parrish, S. V. Viscido, and D. Grünbaum, Biol. Bull. **202**, 296 (2002).
[5] A. Garcimartín, J. M. Pastor, L. M. Ferrer, J. J. Ramos, C. Martín-Gómez, and I. Zuriguel, Phys. Rev. E **91**, 022808 (2015).
[6] M. Chraibi, A. Seyfried, and A. Schadschneider, Phys. Rev. E **82**, 046111 (2010).
[7] F. Fadda, D. A. Matoz-Fernandez, R. Van Roij, and S. Jabbari-Farouji, Soft Matter **19**, 2297 (2023).
[8] S. Roca-Bonet and M. Ripoll, Eur. Phys. J. E **45**, 25 (2022).
[9] H. R. Vutukuri, M. Hoore, C. Abaurrea-Velasco, L. Van Buren, A. Dutto, T. Auth, D. A. Fedosov, G. Gompper, and J. Vermant, Nature (London) **586**, 52 (2020).
[10] G. Volpe, I. Buttinoni, D. Vogt, H.-J. Kümmerer, and C. Bechinger, Soft Matter **7**, 8810 (2011).
[11] L. Giomi, N. Hawley-Weld, and L. Mahadevan, Proc. R. Soc. A. **469**, 20120637 (2013).
[12] J. Deseigne, O. Dauchot, and H. Chaté, Phys. Rev. Lett. **105**, 098001 (2010).
[13] J. Elgeti, R. G. Winkler, and G. Gompper, Rep. Prog. Phys. **78**, 056601 (2015).
[14] C. Bechinger, R. Di Leonardo, H. Löwen, C. Reichhardt, G. Volpe, and G. Volpe, Rev. Mod. Phys. **88**, 045006 (2016).
[15] A. P. Solon, J. Stenhammar, M. E. Cates, Y. Kafri, and J. Tailleur, Phys. Rev. E **97**, 020602(R) (2018).
[16] T. Speck, Phys. Rev. E **103**, 012607 (2021).
[17] J. Stenhammar, A. Tiribocchi, R. J. Allen, D. Marenduzzo, and M. E. Cates, Phys. Rev. Lett. **111**, 145702 (2013).
[18] A. Wysocki, R. G. Winkler, and G. Gompper, Europhys. Lett. **105**, 48004 (2014).
[19] F. Dittrich, T. Speck, and P. Virnau, Eur. Phys. J. E **44**, 53 (2021).
[20] F. Dittrich, J. Midya, P. Virnau, and S. K. Das, Phys. Rev. E **108**, 024609 (2023).

[21] M. Hess, M. Gratz, H. Remmer, S. Webers, J. Landers, D. Borin, F. Ludwig, H. Wende, S. Odenbach, A. Tschöpe, and A. M. Schmidt, Soft Matter **16**, 7562 (2020).
[22] D. L. Braunmiller, S. Babu, D. B. Gehlen, M. Seuß, T. Haraszti, A. Falkenstein, J. Eigen, L. De Laporte, and J. J. Crassous, Adv. Funct. Mater. **32**, 2202430 (2022).
[23] T. Zinn, L. Sharpnack, and T. Narayanan, Soft Matter **19**, 2311 (2023).
[24] F. R. Koessel and S. Jabbari-Farouji, New J. Phys. **22**, 103007 (2020).
[25] F. R. Koessel and S. Jabbari-Farouji, Europhys. Lett. **125**, 28001 (2019).
[26] S. Chatterjee, M. Mangeat, R. Paul, and H. Rieger, Europhys. Lett. **130**, 66001 (2020).
[27] M. Abkenar, K. Marx, T. Auth, and G. Gompper, Phys. Rev. E **88**, 062314 (2013).
[28] F. Peruani, A. Deutsch, and M. Bär, Phys. Rev. E **74**, 030904(R) (2006).
[29] R. S. Negi, R. G. Winkler, and G. Gompper, Phys. Rev. Res. **6**, 013118 (2024).
[30] L. Barberis and F. Peruani, Phys. Rev. Lett. **117**, 248001 (2016).
[31] T. Vicsek, A. Czirók, E. Ben-Jacob, I. Cohen, and O. Shochet, Phys. Rev. Lett. **75**, 1226 (1995).
[32] For spherical particles and 3D hydrodynamics, the translational diffusion coefficient is $D_{\mathrm{T}} = k_B \mathrm{T}/\gamma_{\mathrm{T}}$ and the translational drag coefficient $\gamma_{\mathrm{T}} = 6\pi\eta R$, where $k_{\mathrm{B}}$ is the Boltzmann constant, $T$ the absolute temperature, $\eta$ the fluid viscosity, and R the particle radius. The rotational motion of the particle is described by $\dot{\boldsymbol{\varphi}} = \sqrt{2\mathrm{D}_{\mathrm{R}}}\boldsymbol{\xi}_R$ with the rotational diffusion coefficient $D_{\mathrm{R}} = k_{\mathrm{B}}T/\gamma_R$ and the rotational drag coefficient $\gamma_{\mathrm{R}} = 8\pi\eta R^3$.
[33] J. T. Siebert, F. Dittrich, F. Schmid, K. Binder, T. Speck, and P. Virnau, Phys. Rev. E **98**, 030601(R) (2018).
[34] See Supplemental Material at http://link.aps.org/supplemental/10.1103/PhysRevE.111.015425 for videos on domain structure and coarsening, an analysis of the dipole orientation, the comparison of our data for the binodals for $B = 0$ with literature data, the determination of critical-point coordinates using Binder cumulants, details on how to evaluate spatial two-point correlation and autocorrelation functions, further discussion on cluster growth and motion, and an analysis of the interparticle forces..
[35] R. A. Gallardo, O. Idigoras, P. Landeros, and A. Berger, Phys. Rev. E **86**, 051101 (2012).
[36] J. Midya, S. A. Egorov, K. Binder, and A. Nikoubashman, J. Chem. Phys. **151**, 034902 (2019).
[37] S. Hermann, D. De Las Heras, and M. Schmidt, Phys. Rev. Lett. **123**, 268002 (2019).
[38] A. J. Bray, Adv. Phys. **51**, 481 (2002).
[39] I. M. Lifshitz and V. V. Slyozov, J. Phys. Chem. Solids **19**, 35 (1961).
[40] F. Haußer and A. Voigt, Phys. Rev. B **72**, 035437 (2005).
[41] P. W. Voorhees, Annu. Rev. Mater. Sci. **22**, 197 (1992).
[42] S. Paul, A. Bera, and S. K. Das, Soft Matter **17**, 645 (2021).
[43] S. K. Das, J. Chem. Phys. **146**, 044902 (2017).
[44] T. Vicsek and F. Family, Phys. Rev. Lett. **52**, 1669 (1984).
[45] C. B. Caporusso, L. F. Cugliandolo, P. Digregorio, G. Gonnella, D. Levis, and A. Suma, Phys. Rev. Lett. **131**, 068201 (2023).
[46] J. Midya, S. Majumder, and S. K. Das, J. Phys.: Condens. Matter **26**, 452202 (2014).
[47] J. Midya, S. Majumder, and S. K. Das, Phys. Rev. E **92**, 022124 (2015).
[48] C. Yeung, M. Rao, and R. C. Desai, Phys. Rev. E **53**, 3073 (1996).
[49] P. K. Ghosh, V. R. Misko, F. Marchesoni, and F. Nori, Phys. Rev. Lett. **110**, 268301 (2013).
[50] A. P. Thompson, H. M. Aktulga, R. Berger, D. S. Bolintineanu, W. M. Brown, P. S. Crozier, P. J. in 't Veld, A. Kohlmeyer, S. G. Moore, T. D. Nguyen, R. Shan, M. J. Stevens, J. Tranchida, C. Trott, and S. J. Plimpton, Comput. Phys. Commun. **271**, 108171 (2022).
[51] A. Stukowski, Modelling Simul. Mater. Sci. Eng. **18**, 015012 (2010).